

www.acsami.org Research Article

Ultrahigh Brightening of Infrared PbS Quantum Dots via Collective Energy Transfer Induced by a Metal-Oxide Plasmonic Metastructure

Seyed M. Sadeghi,* Rithvik R. Gutha, Ali Hatef, Ryan Goul, and Judy Z. Wu



Cite This: ACS Appl. Mater. Interfaces 2020, 12, 11913–11921



ACCESS More Article Recommendations Supporting Information

🐌 : CdSe/ZnS QD 🏽 🕥 : PbS QD

ABSTRACT: We demonstrate that a solution-processed heterojunction interface formed via the addition of a thin buffer layer of CdSe/ZnS quantum dots (QDs) to a functional metal oxide plasmonic metastructure (FMOP) can set up a collective interquantum dot energy-transport process, significantly enhancing the emission of infrared PbS quantum dots. The FMOP includes a Schottky junction, formed via deposition of a Si layer on arrays of Au nanoantennas and a Si/Al oxide charge barrier. We show when these two junctions are separated from each other by about 15 nm and the CdSe/ZnS quantum dot buffer layer is placed in touch with the Si/Al oxide junction, the quantum efficiency of an upper layer of PbS quantum dots can increase by about 1 order of magnitude. These results highlight a unique energy circuit formed via collective coupling of the CdSe/ZnS quantum dots with the hybridized states of plasmons and diffraction modes of the arrays (surface lattice resonances) and coupling between such resonances with PbS QDs via lattice-induced photonic modes.

KEYWORDS: PbS quantum dots, collective, energy transfer, surface lattice resonances, metallic nanoantennas, plasmons, exciton-plasmon coupling

1. INTRODUCTION

Colloidal lead sulfide (PbS) quantum dots (QDs) have been the focus of significant attention in recent years. A key feature of these QDs is their band gap scalability, which efficiently covers a wide range of the infrared spectrum. This makes them very attractive for photovoltaic applications, including solar cells, detectors, and light sources. 1-3 Another important feature of PbS QDs is the possibility of multiple exciton generation.4 This process can, in principle, create a new horizon for going beyond the Shockley-Queisser efficiency limit, offering a significant improvement in efficiencies of solar cells. Despite such appealing features, some of the intrinsic properties of PbS QDs have hindered their applications. These include their large amount of defect sites, which are progressively increased with interaction with the ambient environment and light^{5,6} and their slow spontaneous emission decay rates.^{7,8} A combination of these features has led to low efficiencies, as fast nonradiative decay processes can easily dominate radiative decay of PbS QDs, leading to limited useful applications. To alleviate these issues, significant research has been devoted toward the application of plasmonic metallic nanoantennas (mANTs), nanocavities, and photonic cavities

to increase the radiative decay rates of PbS QDs. $^{8-11}$ The key aspect of such investigations is to make such decay processes compete better with the nonradiative decay caused by the defect sites. $^{12-16}$

At the device level, suppression of interface recombination caused by the defect sites of PbS QDs is important for the enhancement of solar cell efficiencies. A recent report has shown that this can be done via the application of a CdSe QD buffer layer at the junction between ZnO nanoparticles and PbS quantum dots. Such a layer can optimize carrier concentration and energy band alignment of such a junction, increasing the solar power conversion efficiencies. Solution-processed ZnO/PbS QD solar cells have also been made more efficient by engineering the band alignment of the QD layers

Received: November 22, 2019 Accepted: February 21, 2020 Published: February 21, 2020



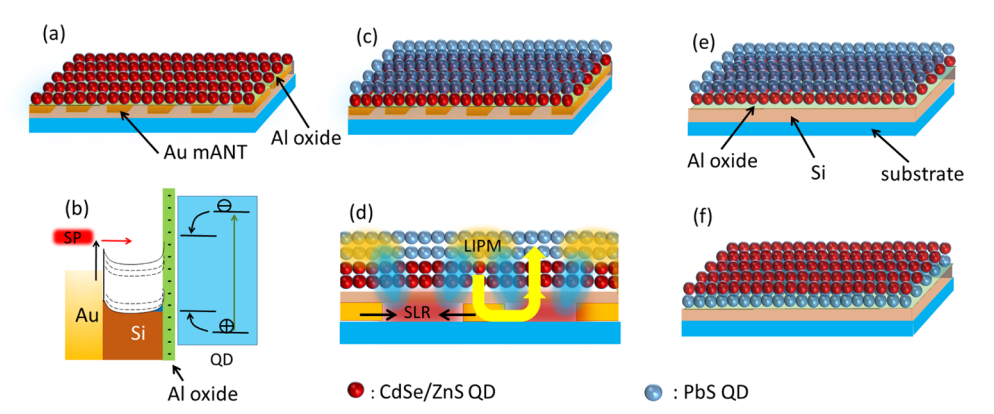


Figure 1. (a) Cross-sectional view of FMOP, including a glass substrate, Au mANT array, Si spacer, an ultrathin Al oxide layer, and a thin film of CdSe/ZnS QDs. (b) Electronics structure of a FMOP, including the Schottky junction and a Si/Al oxide charge barrier. (c) FMOP with a CdSe/ZnS QD buffer and a PbS QD thin film. (d) Schematic illustration of the collective transport of energy from CdSe/ZnS QDs to PbS QDs via SLR and LIPM coupling. Layer arrangements of control samples consisting of CP (e) and PC (f).

through the use of ligand treatments.¹⁸ Additionally, recently the issue of the charge separation at the heterojunction interface of solution-processed PbS/ZnO colloidal QD solar cells was studied.¹⁹ It was shown that photodoping of ZnO quantum dots can increase charge extraction.

Although applications of metallic nanostructures have captured many useful features of plasmonics for enhancement of quantum efficiencies of PbS QDs, this technique is hampered by the inherent loss caused by transfer of energies from the QDs to the mANTs via Forster resonance energy transfer (FRET)²⁰⁻²⁵ and persistent presence of defect sites, referred here as the defect environments (DEs). 26-28 Recently, we presented a platform of material structure, called functional metal oxide plasmonic metastructure (FMOP), that is able to enhance the emission of QDs via Purcell effect while causing plasmon-induced suppression of the DEs (Figure 1a).²⁹ FMOP consisted of an Au/Si Schottky junction close to a Si/Al oxide charge barrier (Figure 1b). The Schottky junction was formed when arrays of mANTs were imbedded in the amorphous Si layer and then a charge barrier was generated by adding an ultranarrow layer of Al oxide (Figure 1a). The plasmoninduced suppression of the DEs in FMOP happens via the generation of hot electrons and their transport across by the Schottky barrier to the Si layer (Figure 1b). In the presence of the Si/Al oxide charge barrier, the captured electrons set up an electrostatic field, suppressing the migration of photoexcited electrons from QDs to surface trap states.

In this paper, we demonstrate that a solution-processed heterojunction interface formed via adding a CdSe/ZnS QD layer (buffer) to a FMOP (Figure 1c) can enhance the emission of efficiencies of thin films of PbS QDs by about 1 order of magnitude. The CdSe/ZnS QD buffer layer is added directly to the top of the Si/Al oxide junction of the FMOP, followed by the deposition of the PbS QDs. We show that the ultrahigh emission enhancement of PbS QD thin films can be associated with a collective energy-transport process that delivers excitation energies from CdSe/ZnS to PbS QDs (Figure 1d). Such a process is involved with the coupling of CdSe/ZnS QDs with surface lattice resonances (SLRs) formed via hybridization of the LSPRs of the mANTs with Rayleigh Anomaly (RA). The periodicity of the mANT array is adjusted such that the SLR wavelengths occur around the excitonic transition energies of the PbS QDs. At the same wavelength range, the array also generates lattice-induced photonic modes

(LIPMs) formed via optical interference. ^{30,31} Our results show that such modes can effectively interact with the PbS QDs and the SLR modes of the mANT arrays. A combination of these processes establishes a coupling between the CdSe/ZnS and PbS QDs, leading to transport of energy from the former to the latter (Figure 1d). These results suggest an energy circuit wherein excitation energy is transported via coupling of two heterogeneous resonances (SLR and LIPMs) and FMOP.

2. METHODOLOGY

Fabrication of FMOP started with the formation of an array of Au mANTs on glass substrates using e-beam lithography. The SEM image of the mANTs (Figure 2a) suggests that the

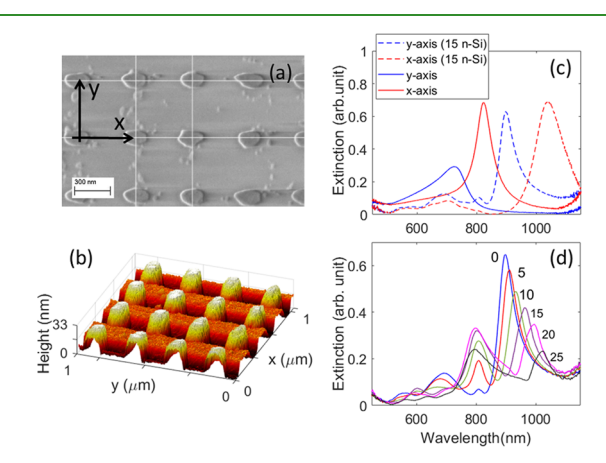


Figure 2. (a) Top-view SEM image of the mANT array before deposition of the Si layer. (b) AFM image of the array after deposition of 15 nm Si. (c) Extinction spectra of the Au array for *x*-pol and *y*-pol when the array is exposed to air (solid lines) and after 15 nm of n-Si deposition (dashed lines). (d) Variation of the extinction spectrum when the sample with 15 nm Si is rotated along the *y*-axis and the incident light has *y*-pol. The number close to each spectrum refers to the angle of rotation. The bar in (a) is 300 nm.

average width of the mANT was 125 nm and the length \sim 200 nm. The nominal height was 40 nm. After this, 15 nm of n-type Si was sputtered on this top of the arrays. Such a doping allows us to have an efficient Schottky barrier for harvesting hot electrons. The AFM image in Figure 2b shows that the 15 nm Si coated the mANTs, leaving the troughs between them open. After this step, 1 nm of Al oxide was sputtered on the top

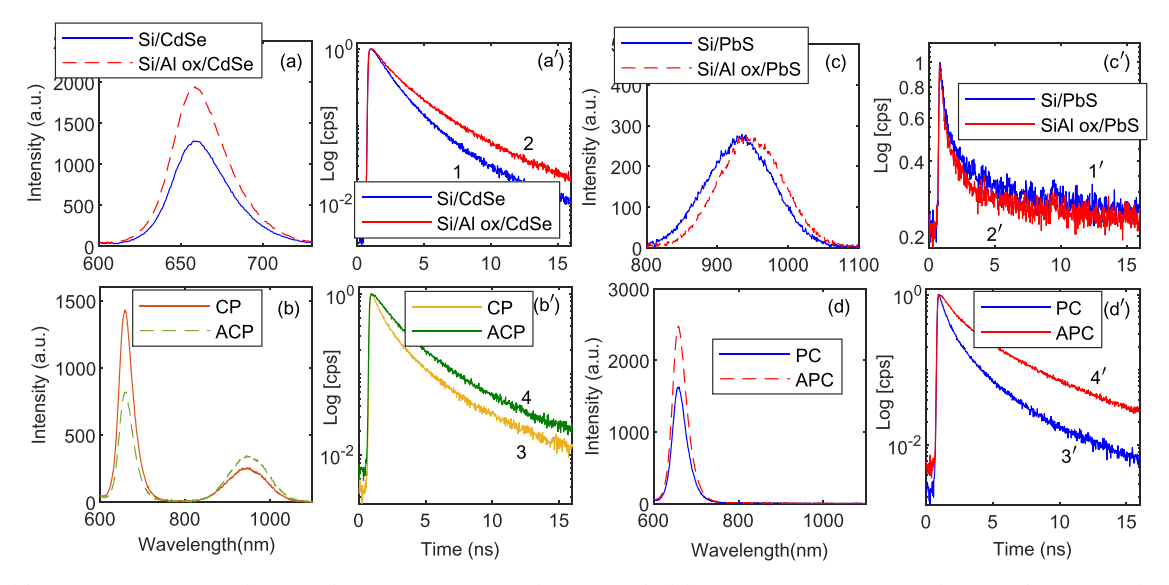


Figure 3. (a) Emission of Si/CdSe (solid line) and Si/Al ox/CdSe (dashed line). (b) Emission of samples, CP (solid line) and ACP (dashed line). (a') shows decay of Si/CdSe (line 1) and Si/Al ox/CdSe (line 2). (b') represents the decay of CdSe/ZnS QDs in samples, CP (line 3) and ACP (line 4). (c) Emission of Si/PbS (solid line) and Si/Al ox/PbS (dashed line). (d) Emission of PC (solid line) and Si/Al ox/PbS/CdSe (dashed line). (c') shows the decay of Si/PbS (line 1') and Si/Al ox/PbS (line 2'). (d') represents the decay of CdSe/ZnS QDs in PC (line 3') and APC (line 4').

of the Si layer. We characterized the properties of the FMOP by spin coating the CdSe/ZnS QDs on the top of the Al oxide and investigate their optical properties. After this step, a solution of PbS QDs was spin-coated on the top of the CdSe/ ZnS QDs (Figure 1c). Several reference samples were also fabricated. These included samples consisting of glass substrates coated with Si and Si/Al oxides with CdSe/ZnS and PbS QD thin films (Figure 1e) and vice versa (Figure 1f). The CdSe/ZnS and PbS QDs were acquired from NN-Labs LLC. The CdSe/ZnS QDs had octadecylamine ligands with core and shell sizes of 4.8 and 4.7 nm, respectively, and they emit at 660 nm. PbS QDs, on the other hand, had oleic acid ligands with 3 nm core sizes, and their emission wavelengths were 920 nm. A laser field with a 514 nm Ar laser was used to excite the QDs, and their emission was detected by sensitive visible and infrared spectrometers. A time-correlated singlephoton counting (TCSPC) system (Picoquant Pico-Timeharp 260) combined with a 30 ps 450 nm pulsed laser and a singlephoton avalanche detector (SPAD) was used to study the lifetimes of these QDs. Because of photoactivities of PbS when they are exposed to air and light, 5,6,33 the measurements were done within few seconds of exposure to the laser beam and immediately after preparation of samples. Note that the 1 nm of Al oxide was formed after exposing the 1 nm of Al to the ambient environment. Our results have shown that this process leads to grains of Al oxide, 34 which expected to have reduced band gaps. 35 Based on our previous reports, 34 1 nm was the optimized thickness for the enhancement of radiative decay of

Figure 2c shows the extinction spectra of the mANT array when the incident light was polarized along x- and y-axes (Figure 2a) referred to as x-pol and y-pol, respectively. The strongly asymmetric peak peaked at 726 nm in the absence of Si in the case of y-pol (blue solid line) refers to the onset of formation of SLR. Adding the Si layer matures the SLR with a peak at about 900 nm (blue dashed line). For the x-pol, the main peaks at 821 nm (no Si) and 1043 nm (with Si) are both associated with the LSPR of individual mANTs. Figure 2d

shows the variation of the extinction spectrum of SLR for *y*-pol when the sample with the Si layer was rotated along the *y*-axis. The results show that rotation splits the main peak in two. The longer wavelength peak shifts quite much with the angle of rotation (θ) . Considering variations of these satellites and the wavelengths of RA (+1,0) and (-1,0) modes with θ (Supporting Information, Figures S1 and S2) confirms the nature of the hybridization of LSPRs with the diffraction modes of the arrays, i.e., the formation of SLRs. This is further confirmed by our numerical simulations in the following pages. A detailed discussion regarding the nature of SLR seen here is provided in the Supporting Information.

3. HETEROJUNCTION INTERFACE CHARACTERIZATION

We start our investigation considering the design of the buffer. For this, we analyzed the emission intensity and dynamics of hybrid structures consisting of CdSe/ZnS and PbS QDs in the presence of glass substrates covered with Si or Si/Al oxide but in the absence of the mANT arrays. For this, we considered two types of arrangements of QDs. As schematically shown in Figure 1e,1f, this includes deposition of CdSe/ZnS QDs followed by PbS QDs, i.e, Si/Al ox/CdSe/PbS (sample ACP), and vice versa, i.e., Si/Al ox/PbS/CdSe (sample APC). Similarly, we considered samples without Al oxide, i.e., Si/ CdSe/PbS (sample CP) and Si/PbS/CdSe (sample PC). We start with the case of Figure 1e. Figure 3a shows the emission of CdSe/ZnS QDs on Si (solid line) and Si/Al oxide (dashed line). The results are along what we reported before, ^{37,38} i.e., an increase in the emission of QDs on Si/Al oxide compared to those directly deposited on Si. The impact of the Al oxide layer on the decay of QDs can be seen in Figure 3a', wherein the Al oxide layer increases the lifetime of CdSe/ZnS QDs (line 2) compared to that without Al oxide (line 1). As discussed by us before, 37,38 this is due to the electrostatic field formed at the Si/Al oxide (charge barrier), that suppresses migration of excitons to the defect sites.³⁹

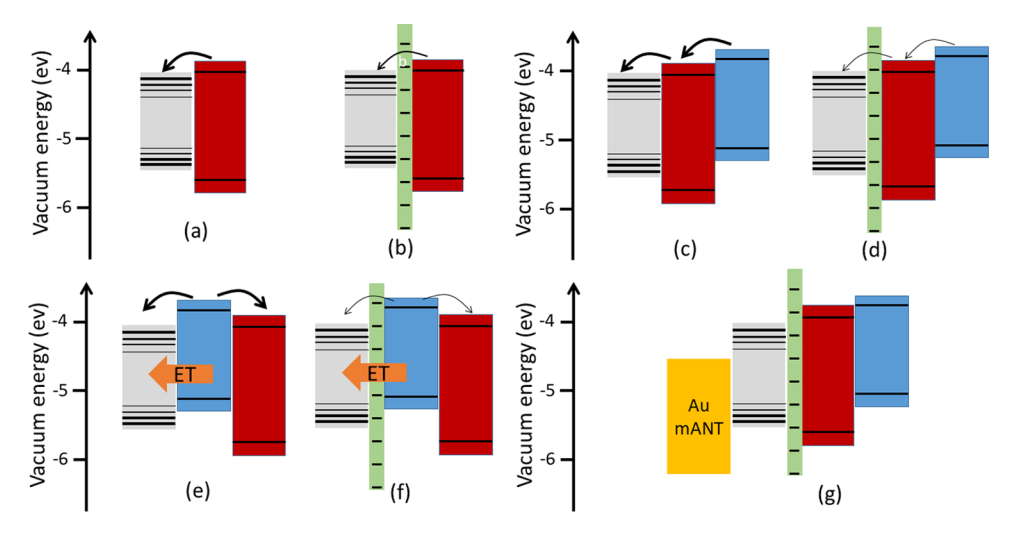


Figure 4. Heterojunction band diagrams of Si/CdSe (a) Si/Al oxide/CdSe (b), CP (c), ACP (d), PC (e), APC (f), and Au-ACP (g). The curved arrows refer to electron-transfer processes and arrows with ET represent FRET from PbS QDs to the Si layer.

The addition of PbS to the top of CdSe/ZnS QDs on such a sample, forming ACP (Figure 1e), offers a different picture. As seen in Figure 3b, for such a configuration we can see the emission of both CdSe/ZnS and PbS QDs at about 660 and ~920 nm, respectively. The results also show that the emission intensities of ACP (dashed line) at 660 nm are about half of that without Al oxide, i.e., CP (solid line). The emission of PbS QDs, on the other hand, has increased with a slight amount of red shift (dashed line). Another key observation is that in this configuration, the lifetime of CdSe/ZnS QDs in the presence of Al oxide (line 4) undergoes a smaller amount of elongation than that of the case without PbS QDs (Figure 3b'). The overall decay rates are, however, faster than those in seen Figure 3a'.

The situation is rather different for the case of APC (Figure 1f). To investigate this, we start with the Si/PbS case. As seen in Figure 3c, the addition of Al oxide (Si/Al ox/PbS system) mostly red shifts the emission spectrum of the PbS QDs (dashed line). Figure 3c' shows adding Al oxide reduces the lifetime of PbS QDs slightly (line 2'). This can be explained, at least in part, considering the fact that the results in Figure 3c' do not represent the overall decay rates of PbS QDs. This is because of the fact that the quantum efficiency of the SPAD of our TCPSC system decreases from 15% at 800 nm to about 2% at 1000 nm. Therefore, for PbS QDs, this system unproportionately detects QDs with smaller core sizes. Since smaller QDs can transfer their energies to QDs with larger cores, their lifetimes are shorter.³¹ Considering this, the red shift seen in Figure 3c (dashed line) pushes the spectrum of PbS QDs further into the longer wavelengths, causing a reduction of a lifetime. To make our measurements more precise in the cases where both types of QDs existed, we used a filter to block the emission of PbS QDs. Note that despite these, a biexponential fitting allows us to show the initial fast decay in Figure 3c', which can be associated with nonradiative decay and has a lifetime of 760 ps for line 1' and 670 ps for the case of line 2'. The details of the fitting processes and the extracted rates can be found in the Supporting Information (Table S1). The slow decay parts, which represent radiative decay, have scales of ~60 and 74 ns. These values are consistent with the fact that PbS QDs can have long radiative

decay due to their degenerate band structures and dielectric screening of excitons. 40,41

Figure 3d shows that the APC configuration supports higher CdSe/ZnS emission than the case of PC. This is rather in contrast to what seen in the case of the ACP system (Figure 3b), wherein we saw a reduction of emission at 660 nm when Al oxide was added. Figure 3d also shows that in both PC and APC systems, there is no sign of emission of the PbS QDs. The lifetimes of the CdSe/ZnS QDs in such a configuration (Figure 3d'), however, offer a significantly longer lifetime (line 4') than that of the case of PC (line 3'). The outcomes of the biexponential fitting of CdSe/ZnS emission (Table S1) show that in the absence of Al oxide (line 3'), the nonradiative and radiative decay time scales are 0.67 and 3.42 ns. In the presence of Al oxide (line 4'), they become 1.41 and 6.32 ns, respectively. Note that this shows that adding Al oxide actually approximately doubles the nonradiative decay lifetime, enabling more radiative decay. Note that the results for CdSe/ZnS and PbS thin films on Si shown in Figure 3a,c can provide some clues regarding the efficiencies of absorption of the laser beam by such thin films. Considering that these films have similar thicknesses (~50 nm), their relative peak heights and widths (Supporting Information, Figure S7) suggest that band-edge exciton densities in CdSe/ZnS QD thin films were about twice of those in PbS QD thin films.

The results presented in Figure 3 can be analyzed considering the electronic states of the QDs and the Si layer. In the case of Figure 3a, note that the defect states in the Si layer can act as acceptors for photoexcited electrons in the CdSe/ZnS QDs (Figure 4a). Therefore, we can associate the increase of the emission with Si/Al ox/CdSe to the fact that the Si/Al oxide surface charge density suppresses the transition of the photoexcited electron in CdSe/ZnS QDs to the Si layer and surface defects of the QDs (Figure 4b). For the case of Figure 3b, the junction alignment of the CP allows the transfer of photoexcited electrons from PbS to CdSe/ZnS QDs and then to the Si layer (Figure 4c). In the presence of the Al oxide, however, the channel of electron transfer to the Si layer from CdSe/ZnS QDs is hampered by the Si/Al oxide charge barrier (Figure 4d). This can lead to some level of optical doping of the CdSe/ZnS QDs, causing suppression of the emission of such QDs via enhancement of Auger recombination. For the case of PbS QDs, however, since they do not have shells, they can be more reactive to the surface passivation caused by Al oxide and irradiation, in general.^{37,38} This may be the reason for the limited increase of intensity, as seen in Figure 3b (dashed line). Note that here we only consider electron migration. Hole-transfer rates are typically smaller than those of electrons,⁴² and for the case of CdSe/ZnS QDs, the shells (ZnS) tend to localize holes more than electrons.⁴³

The results shown in Figure 3c,c' suggest that the Si/Al oxide junction does not have a prominent impact on the emission of PbS QDs. This may be related to initial fast decay seen in the case of such QDs (Figure 3c'). Such a decay is a sign of efficient Auger recombination and a significant presence of trap sites, which may overwhelm the impact of such a junction. For the case of Figure 3d (PC and APC), we can associate the lack of emission of PbS QDs to the multiple decay channels of PbS QDs. As shown in Figure 4e, for such systems, the energies of such QDs can be transferred to the Si layer via FRET. 44 In addition to this, the photoexcited electrons in PbS QDs can readily decay to the Si layer and CdSe/ZnS QDs. A key feature here is the doping of the CdSe/ ZnS QDs via photoexcited transfer from PbS QDs. Such a process can increase the Auger recombination rate in the CdSe/ZnS QDs, causing a reduction of their emission. This process can increase the decay rate of such QDs, as shown in Figure 3d' (line 3'). Considering the results shown in Figure 3d', one expects that adding the Al oxide layer, i.e., forming APC configuration, should allow the electrostatic field of the Si/Al oxide to suppress the migration from the CdSe/ZnS QDs (Figure 4f). The outcome of this can lead to an increase of their emission (Figure 3d, dashed line). Note that here the direct transfer of excitation energy from CdSe/ZnS to PbS QDs (FRET) should not be significant. This is because of the lack of efficient dipole-dipole coupling, as the exciton dipoles of the donors (CdSe/ZnS QDs) have much higher energies than those of the acceptors (PbS QDs).

4. COLLECTIVE ENERGY TRANSFER VIA FMOP

Based on the results presented in Figure 3, the Si/Al ox/CdSe structure seems to have the right heterojunction conditions for emission enhancement of PbS QDs. To see this, we deposited such a structure on the mANT array, forming a FMOP with a CdSe/ZnS buffer layer. This was followed by the spin coating of the PbS QDs on the top (Figure 1c). The alignment of the work functions in such a structure is shown in Figure 4g. As seen in Figure 2c, in such a structure, the LSPRs and SLRs of the mANTs happened at about 650 and 900 nm (blue dashed line), respectively. As a result, CdSe/ZnS QDs are fairly close to LSPRs, while PbS QD transitions happen around the same wavelengths as those of SLRs. The results of measurements of emission of Si/Al ox/CdSe in the absence (solid line) and the presence of Au mANT arrays (dashed line) are shown in Figure 5a. These results show about 4.5 times emission enhancement. Figure 5a' indicates that the decay of Au/Si/Al ox/CdSe is only slightly faster than that of Si/Al ox/CdSe. This is despite the fact that the Purcell effect and FRET from such QDs to mANTs tend to decrease their lifetimes. 16 To see this better, note that the total polarization damping rate of QDs can be expressed as $\gamma_t = \Gamma_r/2 + \Gamma_{nr}/2 + \gamma_p$, wherein Γ_r and $\Gamma_{\rm nr}$ represent the radiative and nonradiative decay rates, respectively, and $\gamma_{\rm p}$ is the pure dephasing rate caused by elastic scattering of excitons with phonons, defects, etc. While the Purcell effect increases Γ_r , the value of Γ_{nr} is the result of decay

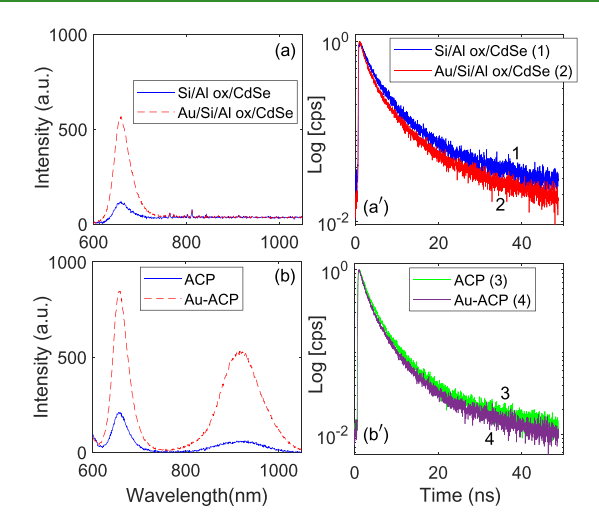


Figure 5. (a) Emission of Si/Al ox/CdSe (solid line) and Au/Si/Al ox/CdSe (dashed line). (b) Emission of ACP (solid line) and Au-ACP (dashed line). (a') shows the decay of CdSe/ZnS QDs in Si/Al ox/CdSe (line 1) and Au/Si/Al ox/CdSe (line 2). (b') represents the decay of CdSe/ZnS QDs in ACP (line 3) and Au-ACP (line 4).

via FRET and defect sites. In the Au/Si/Al ox/CdSe system, the FRET process can increase Γ_{nr} , while the hot-electron-induced passivation of QDs via FMOP reduces this rate. Therefore, depending on the extent of suppression of Γ_{nr} via FMOP, the overall decay rate of the QDs maybe not a direct measure of the Purcell effect and FRET (Supporting Information, Table S1). 28,29,34

The addition of PbS QDs on the top of the FMOP with the CdSe/ZnS QD buffer layer leads to interesting observations. Figure 5b shows the results for the cases of ACP (solid line) and Au/ACP (dashed line), demonstrating that addition of PbS QDs leads to some reduction of the emission enhancement factor of the CdSe/ZnS QDs, decreasing from ~5 in Figure 5a to ~4 in Figure 5b. On the other hand, the emission of PbS QDs undergoes a very high enhancement of about 10 times. These happen without any significant spectral variations. Figure 5b' shows that, despite such significant changes in the emission of the QDs, the ACP and Au/ACP structures support similar decay rates for the CdSe/ZnS QDs (lines 3 and 4).

To discuss the physics behind the results shown in Figure 5, we need to highlight two major features. The first is the carrier relaxation and energy-transport processes in the Au/Si/Al ox/ CdSe/PbS structure and the second is the interaction of CdSe/ ZnS and PbS QDs with the mANT array. To address the latter, we studied the mode profiles and resonances of the array using the COMSOL MultiPhysics software (Supporting Information, Section 3). The results presented in Figure 6a,6b show the extinction spectra when the incident light was considered to be polarized along y- (y-pol) and x-axes (x-pol), respectively. These two figures support strong peaks at 790 (peak C) and 945 nm (peaks C'), respectively. The results also show that peak C is particularly sharp. Each of these spectra also has smaller peaks in the short wavelength sides (peaks A, B, A', and B'). Figure 6c-e shows the mode profile associated with peaks A, B, and C, in the y-z plane, respectively. This plane passes through the middle of the mANT along the y-axis (Figure S3a). Figure 6c'-6e' represents these modes along the in the x-z plane. This plane passes through the middle of the mANT along the x-axis (Figure S3b). Figure 6g,6g' shows the

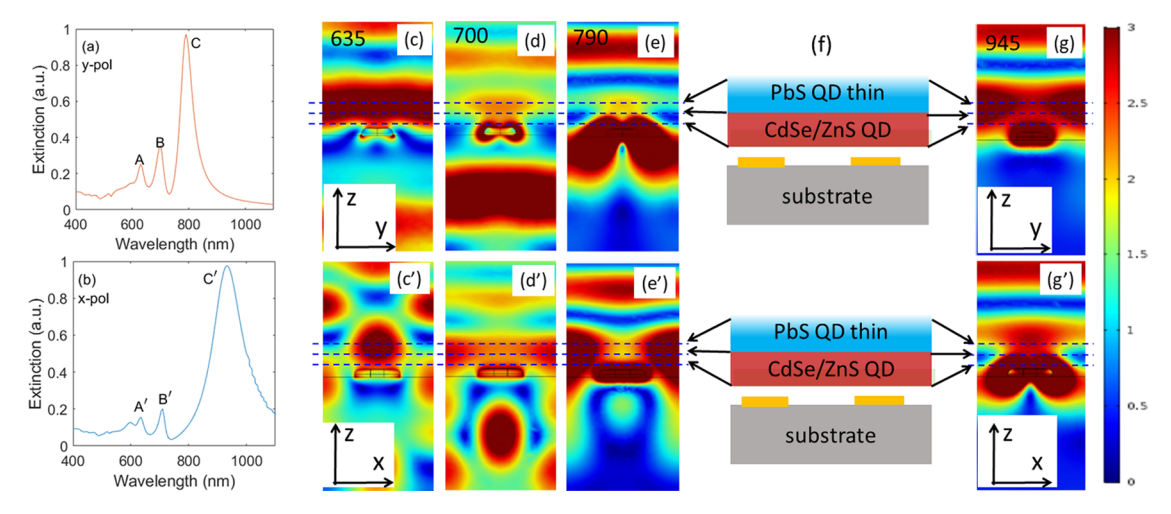


Figure 6. (a, b) represent, respectively, the results of the simulation for transverse (y-pol) and longitudinal (x-pol) extinction spectra of the mANT arrays, as shown in Figure 1a. (c-e) show the mode profiles in the y-z plane for peaks A, B, and C in (a). (c'-e') refer to mode profiles of the same peaks in the x-z plane. (g, g') represent the mode profiles of peak C' in the y-z and x-z planes, respectively. (f) compares the scale of thickness and the position of CdSe/ZnS and PbS QD thin films with the mode profiles.

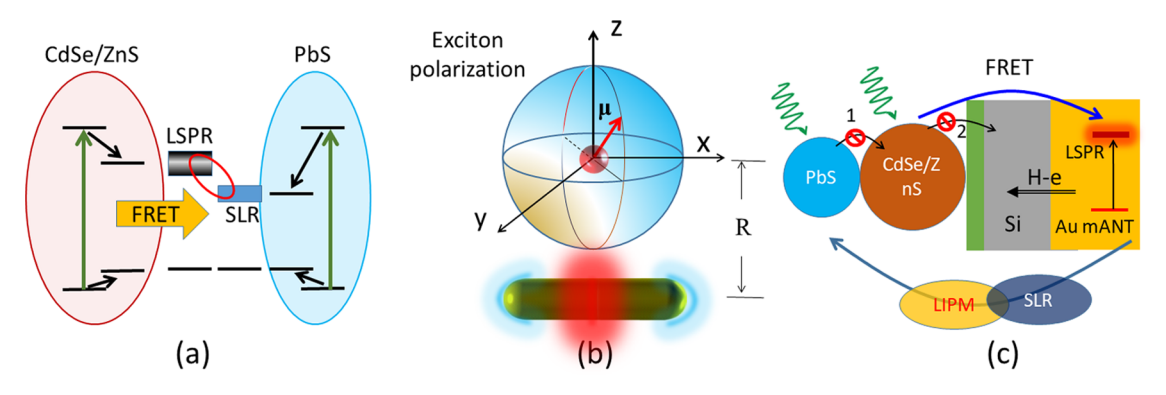


Figure 7. (a) Schematic diagram of electron relaxation, energy-transfer processes, exciton-induced excitation of LSPRs in a Au/ACP system. (b) Exciton dipoles after carrier relaxation in off-resonantly excited QDs and the transverse and longitudinal modes of a mANT. (c) The overall scheme of the energy-transfer route from optical excitation in CdSe/ZnS to PbS QDs.

mode profiles of peak C', i.e., for the x-pol, in the y-z and x-z planes, respectively.

At 635 nm (peak A), the results in Figure 6c show the formation of a strong optical mode on the top of the mANTs. This mode is extended along the y-axis and coupled to the plasmonic edge modes of the mANT in the superstrate, as seen in Figure 6c'. The mode profiles associated with peak B show a stronger plasmonic feature but with less photonics loading (Figure 6d). The optical mode, now is rather mostly extended along the y-axis in the superstrate (Figure 6d'). These results suggest that peak A is a LIPM, involving edge modes and photonic modes generated by the periodicity of the array. 30,31 Peak B is involved with LSPR coupled with the photonic modes. For the case of peak C, we can see the strong optical field between the mANT mostly in the substrate (Figure 6e). This refers to the SLR. Such a resonance is the outcome of the hybridization of the diffraction modes of the mANT arrays with the LSPRs. This happens when the Rayleigh Anomaly wavelength is close to the LSPRs (Supporting Information, Section 1). 36,45,46 As seen in Figure 6e, for the structures considered in this paper, the diffractive coupling of LSPRs mostly occurs in the substrate. Figure 6e' shows this resonance is also coupled with the photonic modes along the y-axis. Such a mode is well inside the superstrate. For the x-pol (longitudinal), the results in Figure 6g,g', suggest that peak

C' is mostly the fundamental longitudinal mode of the mANTs. Note that this mode is accompanied by an intense photonic field in the superstrate.

Figure 6f compares the relative positions of the CdSe/ZnS and PbS QD thin films from the FMOP structure with the spatial positions of the LIPMs and SLR modes in the superstrate. We estimated the thicknesses of the CdSe/ZnS and PbS QDs were about 50 nm. Considering this, for y-pol (Figure 6c-6e,c'-6e') we note that the CdSe/ZnS QD film can well be influenced by the plasmonic fields (transverse LSPRs) of the individual mANTs. This explains the emission enhancement of such QDs via FMOP, as seen in Figure 5a. Additionally, Figure 6e' shows SLRs are clearly coupled with photonic modes (LIPMs) with high overlap with the PbS thin film. Note that the results seen in Figure 6 indicate that the impact of LSPRs on PbS QDs is not significant, as their energies do not match well and the modes associated with LSPRs do not reach the PbS QD thin films.

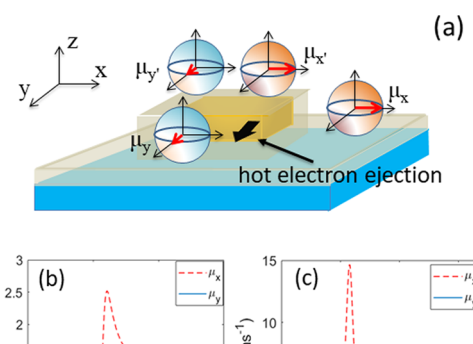
Considering these features and the fact that the wavelength of the laser used to optically excite QDs was 514 nm, the overall alignment of transition energies of the Au/ACP structure is shown in Figure 7a. Note that this figure emphasizes the fact that neither LSPRs nor SLR is directly excited by this laser. Rather such a laser predominantly excites CdSe/ZnS and PbS QDs off-resonantly, which after relaxation

they form near-band gap excitons (Figure 7a). In general, the dipoles of such excitons (μ) have random directions. In the presence of the mANTs, however, the QD dipoles with specific directions (x and y-axes) can interact with the mANTs, exciting transverse or longitudinal plasmon modes (Figure 7b). Based on the transition energies of CdSe/ZnS QDs, we expect such dipoles predominantly interact with transverse modes (y-pol) of the mANTs. Such interaction allows energies of the CdSe/ZnS QDs to be transferred to the LSPRs via FRET. In a recent investigation, we provided some evidence of direct the energy transfer from QDs to LSPRs and SLRs. This was done considering the QDs were biologically conjugated with the mANTs. 47

On the other hand, since the energies of excitons associated with PbS QDs are very close to SLRs (Figure 7a), they can indirectly couple to the SLR mode via LIPMs (Figure 6e'). 31,47 Therefore, the photons emitted by PbS QDs can couple to the SLRs and, in turn, they can enhance the emission of such QDs. A critical feature shown in Figure 7a is the fact that LSPRs are coupled with diffractive modes or RA. This suggests the possibility of linking between CdSe/ZnS and PbS QDs and, therefore, energy sharing. Figure 7c schematically shows the overall picture that can be responsible for the ultrahigh enhancement of the emission of the PbS QDs. The main driver of energy transport depicted in this picture is the interaction of the CdSe/ZnS QDs with the FMOP, which makes such QDs highly efficient emitters. Such QDs also have high absorption efficiency. Such a highly energized system is interacting with PbS QDs via SLR and LIPM, which leads to a flow of energy from CdSe/ZnS to PbS QDs (Figure 1d).

To gain further insight into the physical pictures of the exciton-induced excitation of LSPRs and FRET shown in Figure 7a, note that based on the AFM image shown in Figure 2b, the 15 nm Si layer mostly coated the mANTs. As a result, after spin coating, we expect CdSe/ZnS QDs to fill the troughs between the mANTs. Therefore, such QDs can interact with the mANTs not only from the top but also from the sides (Figure 8a). Based on this picture, we theoretically investigated the interaction of single QDs with a Au mANT to determine which cases provided the most efficient interaction (details are provided in Supporting Information, Section 4). In Figure 8a, $\mu_{x'}$ and $\mu_{y'}$ refer the cases when the QD dipoles were on the top of the mANT with directions along x- and y-axes, respectively. μ_x and μ_y on the other hand, represent the cases of QDs that were placed in the troughs (sides) of the mANTs, also along the x- and y-axes.

Figure 8b shows the plasmonic field enhancement factor $(P_{\text{enh}}, \text{ eq S4})$ for μ_x (dashed line) and μ_y (solid line). Note that the peaks of $P_{\rm enh}$ for this polarization happen at different wavelengths. This is because that μ_x and μ_y excite longitudinal (x-pol) and transverse plasmons (y-pol), respectively. Figure 8c shows the rate of FRET from the QDs to the mANT $(\Gamma_{FRET}, eq S8)$ under these conditions. The results show a high rate for the case of x-pol. Here, however, the important factor is that the longitudinal mode occurs at longer wavelengths. Since in our experiment, the CdSe/ZnS QD exciton energies were close to the y-pol of the mANTs, in practice μ_x was not promoted. The cases of $\mu_{x'}$ (dashed line) and $\mu_{y'}$ offer similar situations, although here the amount P_{enh} and Γ_{FRET} are much less (Figure 8d,e), particularly for the case of y-pol. Considering these results, we can infer that the prominent mechanism of LSPRs was the side coupling of the QDs with the mANT along the y-axis. Such an excitation can be most



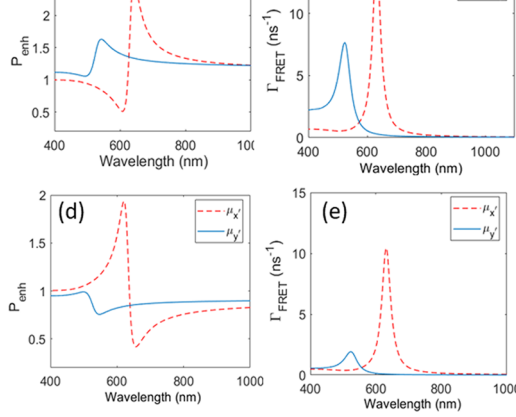


Figure 8. (a) Schematic of projected dipole moments of QDs located on the top $(\mu_{x'}$ and $\mu_{y'})$ and along the sides of a mANT $(\mu_x$ and $\mu_y)$. (b, c) refer to the plasmonic field enhancement and the FRET rate from QDs to mANT for the case of QDs along the side of the mANT and (d, e) represent the case when the QDs were on the top of the mANT.

effective in terms of hot-electron excitation and transfer across the Schottky barrier. In fact, based on refs 48, 49, the hot-electron transfer is influenced by the direction of the incident polarization and becomes quite efficient when the mANT is embedded in the semiconductor, allowing side ejection (Figure 8a). These features further highlight how FMOP can make CdSe/ZnS QDs very optically active, acting as a source of energy that can flow toward the PbS QDs.

5. CONCLUSIONS

We demonstrated the formation of an energy circuit wherein energy was transferred from CdSe/ZnS to PbS QDs. The driver of such an energy-transport process was a metal oxide plasmonic metafilm consisting of a Au mANT array, a Si layer, and an ultrathin layer of Al oxide. We showed in such a structure that the coupling between LSPRs and SLRs brings the excitations of heterojunction caused by these two types of processed-based QDs close to each other. Coupling of the photonic modes caused by the periodicity of the mANT arrays in superstrate with the SLRs combined with the coupling of the LSPRs with RA then allows routing of energy along such a circuit.

ASSOCIATED CONTENT

Supporting Information

The Supporting Information is available free of charge at https://pubs.acs.org/doi/10.1021/acsami.9b20517.

Hybridization of LSPRs and Rayleigh Anomaly and analysis of SLRs in the mANT arrays, biexponential fittings to the QD decays, details of the COMSOL simulations of SLRs and LIPMs, modeling of interaction

of PbS and CdSe/ZnS QDs in the FMOP environment, conversion of the extinction spectra of the mANT arrays and QD emission spectra to energy unit (PDF)

AUTHOR INFORMATION

Corresponding Author

Seyed M. Sadeghi — Department of Physics and Astronomy, University of Alabama in Huntsville, Huntsville, Alabama 35899, United States; o orcid.org/0000-0002-5043-5032; Email: seyed.sadeghi@uah.edu

Authors

Rithvik R. Gutha — Department of Physics and Astronomy, University of Alabama in Huntsville, Huntsville, Alabama 35899, United States; orcid.org/0000-0001-6172-2486

Ali Hatef — Department of Computer Science and Mathematics, Nipissing University, North Bay, Ontario P1B 8L7, Canada Ryan Goul — Department of Physics and Astronomy, University of Kansas, Lawrence, Kansas 66045, United States

Judy Z. Wu – Department of Physics and Astronomy, University of Kansas, Lawrence, Kansas 66045, United States

Complete contact information is available at: https://pubs.acs.org/10.1021/acsami.9b20517

Notes

The authors declare no competing financial interest.

ACKNOWLEDGMENTS

This work is supported by US National Science Foundation under grant number ECCS-1917544. J.Z.W. and R.G. also acknowledge support in part by ARO contract No. W911NF-16-1-0029 and NSF contract Nos. NSF-DMR-1508494, NSF-DMR-1909292, and NSF-ECCS-1809293.

REFERENCES

- (1) Ko, D.-K.; Maurano, A.; Suh, S. K.; Kim, D.; Hwang, G. W.; Grossman, J. C.; Bulovic, V.; Bawendi, M. G. Photovoltaic Performance of PbS Quantum Dots Treated with Metal Salts. ACS Nano 2016, 10, 3382–3388.
- (2) De Iacovo, A.; Venettacci, C.; Colace, L.; Scopa, L.; Foglia, S. Pbs Colloidal Quantum Dot Photodetectors Operating in the Near Infrared. *Sci. Rep.* **2016**, *6*, No. 37913.
- (3) Shulga, A. G.; Kahmann, S.; Dirin, D. N.; Graf, A.; Zaumseil, J.; Kovalenko, M. V.; Loi, M. A. Electroluminescence Generation in PbS Quantum Dot Light-Emitting Field-Effect Transistors with Solid-State Gating. *ACS Nano* **2018**, *12*, 12805–12813.
- (4) Aerts, M.; Suchand Sandeep, C.; Gao, Y.; Savenije, T. J.; Schins, J. M.; Houtepen, A. J.; Kinge, S.; Siebbeles, L. D. Free Charges Produced by Carrier Multiplication in Strongly Coupled PbSe Quantum Dot Films. *Nano Lett.* **2011**, *11*, 4485–4489.
- (5) Tang, J.; Brzozowski, L.; Barkhouse, D. A. R.; Wang, X.; Debnath, R.; Wolowiec, R.; Palmiano, E.; Levina, L.; Pattantyus-Abraham, A. G.; Jamakosmanovic, D.; Sargent, E. H. Quantum Dot Photovoltaics in the Extreme Quantum Confinement Regime: the Surface-Chemical Origins of Exceptional Air-And Light-Stability. ACS Nano 2010, 4, 869–878.
- (6) Choi, H.; Ko, J.-H.; Kim, Y.-H.; Jeong, S. Steric-Hindrance-Driven Shape Transition in PbS Quantum Dots: Understanding Size-Dependent Stability. *J. Am. Chem. Soc.* **2013**, *135*, 5278–5281.
- (7) Tsokkou, D.; Papagiorgis, P.; Protesescu, L.; Kovalenko, M. V.; Choulis, S. A.; Christofides, C.; Itskos, G.; Othonos, A. Photophysics of PbS Quantum Dot Films Capped with Arsenic Sulfide Ligands. *Adv. Energy Mater.* **2014**, *4*, No. 1301547.
- (8) Akselrod, G. M.; Weidman, M. C.; Li, Y.; Argyropoulos, C.; Tisdale, W. A.; Mikkelsen, M. H. Efficient Nanosecond Photo-

- luminescence from Infrared PbS Quantum Dots Coupled to Plasmonic Nanoantennas. ACS Photonics 2016, 3, 1741–1746.
- (9) Wu, K.; Zhang, J.; Fan, S.; Li, J.; Zhang, C.; Qiao, K.; Qian, L.; Han, J.; Tang, J.; Wang, S. Plasmon-Enhanced Fluorescence of PbS Quantum Dots for Remote Near-Infrared Imaging. *Chem. Commun.* **2015**, *51*, 141–144.
- (10) Liang, H.; Zhao, H.; Li, Z.; Harnagea, C.; Ma, D. Silver Nanoparticle Film Induced Photoluminescence Enhancement of Near-Infrared Emitting PbS and Pbs/Cds Core/Shell Quantum Dots: Observation Of Different Enhancement Mechanisms. *Nanoscale* **2016**, *8*, 4882–4887.
- (11) Fushman, I.; Englund, D.; Vučković, J. Coupling of PbS Quantum Dots to Photonic Crystal Cavities at Room Temperature. *Appl. Phys. Lett.* **2005**, *87*, No. 241102.
- (12) Kinkhabwala, A.; Yu, Z.; Fan, S.; Avlasevich, Y.; Müllen, K.; Moerner, W. Large Single-Molecule Fluorescence Enhancements Produced by a Bowtie Nanoantenna. *Nat. Photonics* **2009**, *3*, 654–657.
- (13) Ureña, E. B.; Kreuzer, M. P.; Itzhakov, S.; Rigneault, H.; Quidant, R.; Oron, D.; Wenger, J. Excitation Enhancement of a Quantum Dot Coupled to a Plasmonic Antenna. *Adv. Mater.* **2012**, 24, OP314–OP320.
- (14) Yuan, C.; Wang, Y.; Cheng, H.; Wang, H.; Kuo, M.; Shih, M.; Tang, J. Modification of Fluorescence Properties in Single Colloidal Quantum Dots by Coupling to Plasmonic Gap Modes. *J. Phys. Chem.* C 2013, 117, 12762–12768.
- (15) Russell, K. J.; Liu, T.-L.; Cui, S.; Hu, E. L. Large Spontaneous Emission Enhancement in Plasmonic Nanocavities. *Nat. Photonics* **2012**, *6*, 459–462.
- (16) Hoang, T. B.; Akselrod, G. M.; Argyropoulos, C.; Huang, J.; Smith, D. R.; Mikkelsen, M. H. Ultrafast Spontaneous Emission Source Using Plasmonic Nanoantennas. *Nat. Commun.* **2015**, *6*, No. 7788.
- (17) Zhao, T.; Goodwin, E. D.; Guo, J.; Wang, H.; Diroll, B. T.; Murray, C. B.; Kagan, C. R. Advanced Architecture for Colloidal PbS Quantum Dot Solar Cells Exploiting a CdsS Quantum Dot Buffer Layer. ACS Nano 2016, 10, 9267–9273.
- (18) Chuang, C.-H. M.; Brown, P. R.; Bulović, V.; Bawendi, M. G. Improved Performance and Stability in Quantum Dot Solar Cells through Band Alignment Engineering. *Nat. Mater.* **2014**, *13*, 796.
- (19) Willis, S. M.; Cheng, C.; Assender, H. E.; Watt, A. A. The Transitional Heterojunction Behavior of PbS/ZnO Colloidal Quantum Dot Solar Cells. *Nano Lett.* **2012**, *12*, 1522–1526.
- (20) Govorov, A. O.; Bryant, G. W.; Zhang, W.; Skeini, T.; Lee, J.; Kotov, N. A.; Slocik, J. M.; Naik, R. R. Exciton-Plasmon Interaction and Hybrid Excitons in Semiconductor-Metal Nanoparticle Assemblies. *Nano Lett.* **2006**, *6*, 984–994.
- (21) Kelly, K. L.; Coronado, E.; Zhao, L. L.; Schatz, G. C. The Optical Properties of Metal Nanoparticles: The Influence of Size, Shape, and Dielectric Environment. *J. Phys. Chem. B* **2003**, *107*, 668–677
- (22) Futamata, M.; Maruyama, Y.; Ishikawa, M. Local Electric Field and Scattering Cross Section of Ag Nanoparticles under Surface Plasmon Resonance by Finite Difference Time Domain Method. *J. Phys. Chem. B* **2003**, *107*, 7607–7617.
- (23) Hao, E.; Schatz, G. C. Electromagnetic Fields Around Silver Nanoparticles and Dimers. *J. Chem. Phys.* **2004**, *120*, 357–366.
- (24) Genov, D. A.; Sarychev, A. K.; Shalaev, V. M.; Wei, A. Resonant Field Enhancements from Metal Nanoparticle Arrays. *Nano Lett.* **2004**, *4*, 153–158.
- (25) Kottmann, J. P.; Martin, O. J.; Smith, D. R.; Schultz, S. Plasmon Resonances of Silver Nanowires with a Nonregular Cross Section. *Phys. Rev. B* **2001**, *64*, No. 235402.
- (26) Jones, M.; Lo, S. S.; Scholes, G. D. Quantitative Modeling of the Role of Surface Traps in Cdse/Cds/Zns Nanocrystal Photoluminescence Decay Dynamics. *Proc. Natl. Acad. Sci. U.S.A.* **2009**, *106*, 3011–3016.
- (27) Shu, G.-W.; Lee, W.-Z.; Shu, I.-J.; Shen, J.-L.; Lin, J. C.-A.; Chang, W. H.; Ruaan, R.-C.; Chou, W. C. Photoluminescence of

- Colloidal Cdse/Zns Quantum Dots Under Oxygen Atmosphere. *IEEE Trans. Nanotechnol.* **2005**, *4*, 632–636.
- (28) Sadeghi, S. M.; Wing, W. J.; Gutha, R. R.; Capps, L. Control of Spontaneous Emission of Quantum Dots Using Correlated Effects of Metal Oxides and Dielectric Materials. *Nanotechnology* **2017**, *28*, No. 095701.
- (29) Sadeghi, S. M.; Wing, W. J.; Gutha, R. R.; Goul, R. W.; Wu, J. Z. Functional Metal-Oxide Plasmonic Metastructures: Ultrabright Semiconductor Quantum Dots with Polarized Spontaneous Emission and Suppressed Auger Recombination. *Phys. Rev. Appl.* **2019**, *11*, No. 024045.
- (30) Sadeghi, S. M.; Gutha, R. R.; Hatef, A. Super-Plasmonic Cavity Resonances in Arrays of Flat Metallic Nanoantennas. *J. Opt.* **2019**, *21*, No. 035001.
- (31) Sadeghi, S. M.; Gutha, R. R.; Sharp, C.; Hatef, A. Mapping Lattice-Induced Plasmon Modes in Metallic Nanoantenna Arrays Using Fluorescence Decay of Semiconductor Quantum Dot Bioconjugates. *Opt. Mater.* **2018**, *85*, 356–362.
- (32) Sadeghi, S. M.; Gutha, R. R.; Wilt, J. S.; Wu, J. Z. Design of Schottky Barrier for Plasmon-Induced Hot-Electron Passivation of Defect Environments of Semiconductor Quantum Dots. *J. Phys. D: Appl. Phys.* **2020**, *53*, No. 115103.
- (33) Sadeghi, S. M.; Nejat, A.; Weimer, J. J.; Alipour, G. Chromium-Oxide Enhancement of Photo-Oxidation of Cdse/Zns Quantum Dot Solids. *J. Appl. Phys.* **2012**, *111*, No. 084308.
- (34) Sadeghi, S. M.; Wing, W. J.; Gutha, R. R.; Wilt, J. S.; Wu, J. Z. Balancing Silicon/Aluminum Oxide Junction for Super-Plasmonic Emission Enhancement of Quantum Dots via Plasmonic Metafilms. *Nanoscale* **2018**, *10*, 4825–4832.
- (35) Sellner, S.; Gerlach, A.; Kowarik, S.; Schreiber, F.; Dosch, H.; Meyer, S.; Pflaum, J.; Ulbricht, G. Comparative Study of the Growth of Sputtered Aluminum Oxide Films on Organic and Inorganic Substrates. *Thin Solid Films* **2008**, *516*, 6377–6381.
- (36) Sadeghi, S. M.; Gutha, R. R.; Wing, W. J. Turning on Plasmonic Lattice Modes in Metallic Nanoantenna Arrays via Silicon Thin Films. *Opt. Lett.* **2016**, *41*, 3367–3370.
- (37) Patty, K.; Sadeghi, S.; Nejat, A.; Mao, C. Enhancement of Emission Efficiency of Colloidal Cdse Quantum Dots on Silicon Substrate via an Ultra-Thin Layer of Aluminum Oxide. *Nanotechnology* **2014**, *25*, No. 155701.
- (38) Patty, K.; Sadeghi, S. M.; Campbell, Q.; Hamilton, N.; West, R. G.; Mao, C. Probing the Structural Dependency of Photoinduced Properties of Colloidal Quantum Dots Using Metal-Oxide Photo-Active Substrates. *J. Appl. Phys.* **2014**, *116*, No. 114301.
- (39) Hoex, B.; Heil, S. B. S.; Langereis, E.; van de Sanden, M. C. M.; Kessels, W. M. M. Ultralow Surface Recombination of C-Si Substrates Passivated by Plasma-Assisted Atomic Layer Deposited Al₂O₃. *Appl. Phys. Lett.* **2006**, *89*, No. 042112.
- (40) Moreels, I.; Lambert, K.; Smeets, D.; De Muynck, D.; Nollet, T.; Martins, J. C.; Vanhaecke, F.; Vantomme, A.; Delerue, C.; Allan, G.; Hens, Z. Size-Dependent Optical Properties of Colloidal PbS Quantum Dots. ACS Nano 2009, 3, 3023–3030.
- (41) Saran, R.; Curry, R. J. Lead Sulphide Nanocrystal Photodetector Technologies. *Nat. Photonics* **2016**, *10*, 81.
- (42) Knowles, K. E.; Peterson, M. D.; McPhail, M. R.; Weiss, E. A. Exciton Dissociation Within Quantum Dot-Organic Complexes: Mechanisms, Use as a Probe of Interfacial Structure, and Applications. *J. Phys. Chem. C* **2013**, *117*, 10229–10243.
- (43) Zhu, H.; Song, N.; Lian, T. Controlling Charge Separation and Recombination Rates in CdSe/ZnS Type I Core-Shell Quantum Dots by Shell Thicknesses. *J. Am. Chem. Soc.* **2010**, *132*, 15038–15045.
- (44) Tabernig, S. W.; Daiber, B.; Wang, T.; Ehrler, B. Enhancing Silicon Solar Cells with Singlet Fission: The Case for FÖRster Resonant Energy Transfer Using a Quantum Dot Intermediate. *J. Photonics Energy* **2018**, *8*, No. 022008.
- (45) Kravets, V. G.; Kabashin, A. V.; Barnes, W. L.; Grigorenko, A. N. Plasmonic Surface Lattice Resonances: A Review of Properties and Applications. *Chem. Rev.* **2018**, *118*, 5912–5951.

- (46) Rodriguez, S. R. K.; Abass, A.; Maes, B.; Janssen, O. T.; Vecchi, G.; Rivas, J. G. Coupling Bright and Dark Plasmonic Lattice Resonances. *Phys. Rev. X* **2011**, *1*, No. 021019.
- (47) Sadeghi, S. M.; Gutha, R. R.; Sharp, C.; Hatef, A. Collective and Local Energy Transfer in Biologically-Hybridized Systems of Semi-conductor Quantum Dots and Metallic Nanoantenna Arrays. *J. Phys. D: Appl. Phys.* **2018**, *51*, No. 415301.
- (48) Hong, T.; Chamlagain, B.; Hu, S.; Weiss, S. M.; Zhou, Z.; Xu, Y.-Q. Plasmonic Hot Electron Induced Photocurrent Response at MoS₂-Metal Junctions. *ACS Nano* **2015**, *9*, 5357–5363.
- (49) Knight, M. W.; Wang, Y.; Urban, A. S.; Sobhani, A.; Zheng, B. Y.; Nordlander, P.; Halas, N. J. Embedding Plasmonic Nanostructure Diodes Enhances Hot Electron Emission. *Nano Lett.* **2013**, *13*, 1687–1692.